optica

Recent advances in planar optics: from plasmonic to dielectric metasurfaces

Patrice Genevet,[1,4] Federico Capasso,[2,*] Francesco Aieta,[3] Mohammadreza Khorasaninejad,[2] and Robert Devlin[2]

[1]Université Côte d'Azur, CNRS, CRHEA, rue Bernard Gregory, Sophia Antipolis 06560 Valbonne, France
[2]John A. Paulson School of Engineering and Applied Sciences, Harvard University, Cambridge, Massachusetts 02138, USA
[3]Hewlett-Packard Laboratories, Palo Alto, California 94304, USA
[4]e-mail: Patrice.genevet@crhea.cnrs.fr
*Corresponding author: capasso@seas.harvard.edu

This article reviews recent progress leading to the realization of planar optical components made of a single layer of phase shifting nanostructures. After introducing the principles of planar optics and discussing earlier works on subwavelength diffractive optics, we introduce a classification of metasurfaces based on their different phase mechanisms and profiles and a comparison between plasmonic and dielectric metasurfaces. We place particular emphasis on the recent developments on electric and magnetic field control of light with dielectric nanostructures and highlight the physical mechanisms and designs required for efficient all-dielectric metasurfaces. Practical devices of general interest such as metalenses, beam deflectors, holograms, and polarizing interfaces are discussed, including high-performance metalenses at visible wavelengths. Successful strategies to achieve achromatic response at selected wavelengths and near unity transmission/reflection efficiency are discussed. Dielectric metasurfaces and dispersion management at interfaces open up technology opportunities for applications including wavefront control, lightweight imaging systems, displays, electronic consumer products, and conformable and wearable optics.   © 2017 Optical Society of America

OCIS codes: (240.0240) Optics at surfaces; (160.3918) Metamaterials; (050.5080) Phase shift; (160.4236) Nanomaterials; (080.3630) Lenses; (120.5060) Phase modulation.

https://doi.org/10.1364/OPTICA.4.000139

1. METASURFACES

Conventional optical components control light using gradual phase accumulation through propagation in refractive materials [1,2]. Diffracting devices rely, to control light, on either gradual phase accumulation or on local phase shifts induced by optical antennas with designed properties or, more generally, by subwavelength scale optical components. Starting from a seminal proposal by Kock to locally reduce the phase velocity of light using subwavelength metallic patches [3], followed by Stork et al. and Farn to realize grating structures with a period small compared with the wavelength of light [4,5], the concept of high-contrast subwavelength (HCG) dielectric structures has led to the development of ultrathin optical components. By varying the material composition, i.e., by variation of the duty cycle of the grating, one can create artificial materials with unconventional properties. Designing the diffracting properties at the subwavelength scale using spatially varying nanostructures, Lalanne et al. reported blazed gratings at red wavelengths with efficiencies greater than 80% at relatively large diffraction angles and preliminary results on lenses in the near IR [6–8].

In parallel to the advances in subwavelength dielectric arrays for visible applications, important progress was made in the microwave with metallic subwavelength reflectarrays or transmitarrays. These are made of metallic resonant patches or antennas [9–12] that can alter the characteristic of microwave radiation.

Recently, ultrathin optical interfaces have been proposed for mid-IR and optical wavelengths [13–24]. These devices, called metasurfaces, rely on the scattering properties of ultrathin subwavelength scale optical resonators patterned at interfaces to control the polarization, phase, amplitude, and dispersion of light. The design was influenced by the ability to control scattering of light from wavelength scale dielectric or metallic nanoparticles in the resonant scattering regime or in the non-resonant one using the geometric phase (see early works from Berry [25], Pancharatnam [26], and Hasman's group [27–29]).

Composed of nanostructures designed and arranged in specific patterns at the interface between two media, these ultrathin optical metasurfaces are able to alter every single aspect of transmitting or reflecting light beams. Their basic operation principle is essentially related to the collective scattering of light by an ensemble of subwavelength optical elements (such as optical antennas, resonators, etc.) with different spectral and polarization responses. Based on this concept, various metasurfaces with interesting optical functionalities have already been realized. Some of the most

significant examples in the literature are metasurfaces to achieve arbitrary reflection and refraction [13,30,31], to focus light and/or control its polarization [27,32–34], to exhibit strong photonic spin Hall effect [35–38], or, for example, to project holographic images [39–41]. Any planar and ultrathin array of optical components made of optical elements that possesses specific electromagnetic response, such as bandpass and stop band frequency selective surfaces, frequency selective perfect absorbers, or perfect magnetic conductors, can also be considered a metasurface [42–47]. Therefore, the field of metasurfaces has rapidly and considerably expanded during the past few years to a point that making a complete review would be beyond the scope of this paper (interested readers could refer to the reviews in [48–50]). Our focus is primarily on the recent progress on metasurfaces given their relevance for practical applications. Metasurface components, which were initially limited in terms of throughput efficiencies, have progressed to the point that it is now possible to design efficient wavefront shaping metasurfaces with performance comparable to state-of-the-art commercial optical components.

The classical Huygens' construction presented in Fig. 1(a) states that every point on a wavefront is a source of secondary wavelets that spread out in the forward direction. The new wavefront is found by constructing the surface tangent to the secondary wavelets. On a metasurface, secondary waves interfere in such a way that their envelopes can now create any arbitrary user-defined wavefront.

The schematic in Fig. 1(b) illustrates the response of a metasurface that refracts light at a controllable angle in the plane of incidence. Here the phase gradient along the intersection between the plane of incidence and the metasurface is designed to be a constant. It can be shown that phase gradient metasurfaces refract light in accordance with the generalized laws of refraction, which can be obtained from an application of Fermat's principle [16]:

$$\begin{cases} \cos \theta_t \sin \varphi_t = \frac{\lambda_0}{2\pi \cdot n_t} \frac{\partial \phi}{\partial x}, \\ n_t \sin \theta_t - n_i \sin \theta_i = \frac{\lambda_0}{2\pi} \frac{\partial \phi}{\partial z}, \end{cases} \quad (1)$$
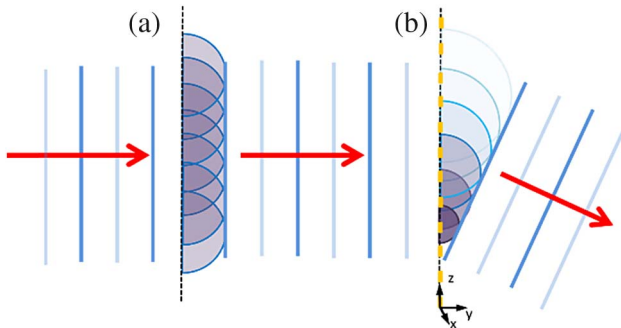

Fig. 1. (a) According to Huygens' construction, each element of a wavefront may be regarded as the center of a secondary disturbance that gives rise to spherical wavelets; the position of the wavefront at any later time is given by the envelope of all such wavelets [51]. (b) Through the introduction of phase shifts for each spherical wavelet by means of sub-wavelength spaced and thick optical elements, the wavefront at any time later can be designed to have any desired profile. In our schematic, the retardations vary in a form of a linear gradient along the plane of incidence in the z direction (meaning that $\frac{\partial \phi}{\partial x} = 0$) to refract light at user-defined angles in the plane of incidence. Note that in this schematic, we have assumed that there is no reflected light. This is correct if the metasurface is impedance matched. Such interfaces are dubbed Huygens metasurfaces and have been proposed and realized in [52].

and similarly reflect light according to the generalized laws of reflection [16]:

$$\begin{cases} \cos \theta_r \sin \varphi_r = \frac{\lambda_0}{2\pi \cdot n_i} \frac{\partial \phi}{\partial x}, \\ \sin \theta_r - \sin \theta_i = \frac{\lambda_0}{2\pi \cdot n_i} \frac{\partial \phi}{\partial z}, \end{cases} \quad (2)$$

where n_i, n_t are the refractive indices of the medium where light is incident and transmitted, respectively, and λ_0 is the vacuum wavelength. In these equations, the directions of the reflected and refracted wavevectors are characterized by the angles $\theta_{r,t}$ (the angle between the reflected/refracted wavevector and its projection on the x–y plane) and $\varphi_{r,t}$ (the angle formed by the projection of the reflected/refracted wavevector on the x–y plane and the y axis) as discussed in detail in [16]. Physically, one can interpret the phase gradient as an effective wavevector, leading to a generalization of the conservation of the wavevector parallel to the surface. This is easily seen from Eq. (1): when the phase gradient lies along the plane of incidence ($\frac{\partial \phi}{\partial x} = 0$), it reduces to Snell's law when $\frac{\partial \phi}{\partial z} = 0$. Note that when the phase gradient does not lie in the plane of incidence, i.e., $\frac{\partial \phi}{\partial x} \neq 0$; $\frac{\partial \phi}{\partial z} \neq 0$, then the reflected and refracted beams are non-coplanar with the incident beam.

It is worth noting that the suppression of certain diffraction orders typical of gradient metasurfaces is also a characteristic of blazed gratings. Their surface is corrugated in a sawtooth manner to provide a constant propagation phase gradient to the diffracted beam. Their diffractive behavior is described by the second of Eqs. (1) as discussed in [53]. Gradient phased metasurfaces can therefore be regarded functionally as ultrathin blazed gratings but with far greater functionality and design potential, because the dispersion of the metasurface optical elements can be engineered to achieve broadband response [22]. Earlier works on metasurfaces have utilized various metallic nanostructures with different shapes and orientations. In metallic nanostructures, resonant scattering of light by oscillating free electrons at the surface occurs due to a resonant electronic–electromagnetic oscillation known as localized plasmonic resonance (LPR). This LPR has been extensively studied previously for creating high electromagnetic field enhancement and has important applications for chemical and biological sensing. It can be described as a radiating metallic antenna. The rigorous treatment of time harmonic radiation of thin-wire antennas involves the solution of the electric field integral equation [54]. To the extent that the metallic nanostructure and the corresponding LPR can be roughly described by a single harmonic oscillator, the scattering phase shift cannot exceed π. We are describing the LPR using a simple model in which it is represented by charge q located at $x(t)$ with mass m on a spring with spring constant k driven by an harmonic incident electric field with frequency ω [55]. This model accurately describes the near- and far-field spectral features of plasmonic resonance, including phase response. Because of the ohmic losses, the charge experiences internal damping with damping coefficient γ:

$$\frac{d^2 x}{dt^2} + \frac{\gamma}{m} \frac{dx}{dt} + \frac{k}{m} x = \frac{q}{m} E_0 e^{i\omega t} + \frac{2q^2}{3mc^3} \frac{d^3 x}{dt^3}. \quad (3)$$

In addition to internal damping, which is proportional to the velocity $\frac{dx}{dt}$, the charge experiences an additional damping force due to radiation reaction that is proportional to the time derivative of the acceleration $\frac{d^3 x}{dt^3}$. This term describes the recoil that the charge feels when it emits radiation, and is referred to as the

Abraham–Lorentz force or simply the radiation reaction force [2]. By assuming harmonic motion $(t) = x_0 e^{i\omega t}$, we can write the steady-state solution to Eq. (3) as

$$x(t) = \frac{AE_0}{(\omega_0^2 - \omega^2) + i(\omega\Gamma_a + \omega^3\Gamma_s)} e^{i\omega t}, \quad (4)$$

where we replace the quantities q, k, m, and γ with more general oscillator parameters $A = \frac{q}{m}$, $\omega_0 = \sqrt{k/m}$, $\Gamma_a = \frac{\gamma}{m}$, and $\Gamma_s = \frac{2}{3}\frac{q^2}{mc^3}$, where Γ_a and Γ_s describe the non-radiative and radiative damping mechanisms, respectively. From Eq. (4) one then sees that the amplitude of the oscillation is in phase with the incident field for $\omega \to 0$ and is phase delayed by π for $\omega \to \infty$, acquiring all intermediate values as the frequency of the signal is swept across the resonance and, in particular, a value of $\pi/2$ when $\omega = \omega_0$. The inability to achieve a phase coverage of 2π varying only ω_0, plus the concomitant problems of poor forward scattering amplitude, and high optical losses at wavelengths shorter than the mid-IR lead to the conclusion that plasmonic metasurfaces using only resonant scattering are not suitable for full wavefront control with high scattering efficiency. Devices using plasmonic resonators are generally hybrid devices, in the sense that they make use of Berry–Pancharatnam (BP) phase [25,26], known also as geometric phase, and of resonant phase delays. In Ref. [13], for example, four v-shaped plasmonic elements are designed to produce a controllable phase retardation in cross polarization over the π-phase range. The design is completed by four identical but $\pi/2$-rotated elements such that each of these scatters light in cross polarization with an additional π retardation. The array of $4 + 4$ elements can therefore cover the entire 2π range. The additional phase delay obtained by converting the polarization with a rotated anisotropic element can be understood by considering rigorous Jones matrix analysis [56]. Let us, for example, consider the reflection from a generic metasurface, representing a two-dimensional array of identical but anisotropic plasmonic resonators illuminated by an incident plane wave. The transmission properties of the interface can then be characterized by the Jones matrix $\boldsymbol{T} = \begin{pmatrix} t_{uu} & t_{uv} \\ t_{vu} & t_{vv} \end{pmatrix}$, where $\hat{u}$ and $\hat{v}$ denote the principal axes of the shape-birefringent nanostructures. Suppose that light is normally incident with a circular polarization with unit vectors defined by $\hat{e}_\pm(0) = \frac{\hat{u} \pm i\hat{v}}{\sqrt{2}}$; we can express the transmission matrix in the new basis in terms of the Pauli matrices $\{\hat{\sigma}_1, \hat{\sigma}_2, \hat{\sigma}_3\}$ and the identity matrix $\hat{I}$ as

$$\boldsymbol{T}(0) = \frac{1}{2}(t_{uu} + t_{vv})\hat{I} + \frac{i}{2}(t_{uv} - t_{vu})\hat{\sigma}_3 + \frac{1}{2}(t_{uu} - t_{vv})\hat{\sigma}_1$$
$$+ \frac{1}{2}(t_{uv} + t_{vu})\hat{\sigma}_2. \quad (5)$$

Now consider the case of a generic resonator rotated in the plane of the metasurface by an angle ϕ with respect to the reference direction $(\phi = 0)$. The transmission matrix is then given by $\boldsymbol{T}(\phi) = \boldsymbol{M}^\dagger(\phi)\boldsymbol{T}(0)\boldsymbol{M}(\phi)$, where $\boldsymbol{M}(\phi) = e^{i\phi\hat{\sigma}_3}$, leading to [56]

Fig. 2. This table summarizes different solutions proposed to address wavefront control with metasurfaces. In the top panel from (a)–(c), the optical response of the nanostructures is tailored by changing the geometry of each individual resonator forming the metasurface. Metasurfaces based on resonance tuning of dielectrics can achieve a phase coverage up to 2π using TE and TM modes, while resonant tuning metasurfaces based on thin plasmonic rod antennas cannot cover the entire 2π phase range. From (d)–(g), metasurfaces based on the PB phase present very high scattering efficiencies, both in reflection and in transmission. PB metasurfaces must, however, be addressed with circularly or elliptically polarized light. (h)–(k) Metasurfaces that work by using both resonant tuning and PB phase tuning have also been demonstrated. (a) is adapted from [31], (b) is adapted from [57], (c) is adapted from [58], (d) is adapted from [18], (e) is adapted from [59], (f) is adapted from [60], (g) is adapted from [27], (h) is adapted from [13], (i) is adapted from [19], (j) is adapted from [61], and (k) is adapted from [33].

$$T(\phi) = \frac{1}{2}(t_{uu} + t_{vv})\hat{I} + \frac{i}{2}(t_{uv} - t_{vu})\hat{\sigma}_3$$
$$+ \frac{1}{2}(t_{uu} - t_{vv})(e^{-i2\phi}\hat{\sigma}_+ + e^{i2\phi}\hat{\sigma}_-)$$
$$+ \frac{1}{2}(t_{uv} + t_{vu})(-e^{-i2\phi}\hat{\sigma}_+ + e^{i2\phi}\hat{\sigma}_-) \qquad (6)$$

after defining the spin–flip operators $\hat{\sigma}_\pm = (\hat{\sigma}_1 \pm i\hat{\sigma}_2)/2$. This notation is very convenient. It helps understand the origin of the so-called PB phase retardation. Spin–flip comes with an additional phase retardation equal to $\pm 2\phi$, which is in fact related to the non-commutation between $e^{i\phi\hat{\sigma}_3}$ and $\hat{\sigma}_\pm$. This calculation can be performed also in reflection mode and helps understand the properties of reflectarray metasurfaces.

In Fig. 2 we classify the different mechanisms used to design metasurfaces. Resonance tuning means that the response of the nanostructures is controlled by the size, with the scattered light polarized with the same polarization of the incident radiation. In order to achieve a large scattering cross section, PB planar (i.e., much thinner than the wavelength) elements need to be resonantly excited, but the phase tuning mechanism remains totally decoupled from the spectral tuning of the resonators [25,26]. Non-resonant strategies have been proposed, in particular, using subwavelength arrays of nanofins with high aspect ratio [Figs. 2(f) and 2(g)]. As will be described later in greater detail, these subwavelength long waveguides act as non-resonant phase shifting elements due to their structural birefringence associated with the anisotropic effective refractive index [14,60,62,63]. These designs lead to high scattering efficiency. Concerning the first column of Fig. 2 on plasmonic metasurfaces, for anisotropic plasmonic resonators in particular that combine resonant tuning with PB, the excitation of plasmonic resonance induces an electric current sheet that radiates on both sides of the interface. To control independently reflection and transmission properties, one needs to make use of several layers [64–68]. By introducing a physical polarization current produced by an aperiodic distribution of polarizable particles exhibiting both electric and magnetic responses, it becomes possible to generate linear, circular, or elliptical polarization from a given excitation without reflections [52].

2. DIELECTRIC METASURFACES AND HIGH CONTRAST GRATINGS

Previously discussed limitations of plasmonic metasurfaces can be overcome by replacing metals with all-dielectric resonators. Dielectric metasurfaces consist of interfaces patterned with a distribution of high-index dielectric light scattering particles of size comparable to the wavelength of light. Their scattering properties were first studied by Faraday [69] and the effect is also known as Faraday–Tyndall scattering. For spherical or cylindrical particles, boundary conditions allow for the separation of the Helmholtz equation, which therefore supports radially and angularly dependent solutions. This separable boundary value problem was first solved by Mie [70]. Exact Mie calculations, also valid for metallic spherical nanoparticles, become very useful for dielectric particles. By expanding the solution into spherical vector wave functions, it is possible to calculate both the radiating and the internal fields. Analytical expressions of the former are generally compared to experimental data and can be fitted to extract contributions of each mode, while the latter represents the field distribution inside the dielectrics. This modal decomposition is

particularly useful in revealing the physical mechanisms at the origin of high metasurface transmissivity or reflectivity.

Interestingly, sufficiently small spherical dielectric nanoparticles provide pronounced resonances associated with the excitation of both magnetic and electric dipolar modes (Figs. 3 and 4). Under certain conditions described by Mie, the first resonance that roughly arises when the effective wavelength is of the order of the particle diameter ($\lambda_0/n_{sp} \approx D_{sp}$) is a magnetic dipole resonance [70]. It is worth pointing out that, unlike split ring resonator (SRR) magnetic resonances, dipolar magnetic resonances in high index dielectric resonators are essentially excited by the electric field and not by the magnetic contribution. Strong magnetic response has been reported, for example, in SiC at mid-IR frequencies [76]. The existence of this condition is characterized for spherical particles by an antiparallel electric field polarization within the sphere, which induces circulating displacement currents and the appearance of a strong magnetic dipole at the center of the particle. For high-refractive-index nanoparticles of diameter around 100–200 nm, these resonances occur in the visible spectral range. As it has been pointed out in [77,78], the magnetic activity of dielectric nanoparticles is due to the curl of the displacement current and, unlike in plasmonic materials, is not associated with large non-radiative losses. It is worth noticing that the polarization of the electric field in a metallic split-ring resonator is antiparallel at each opposite side of the ring and can also efficiently couple to circulating displacement currents [Fig. 3(a)]. These resonators, which have been proposed as building blocks
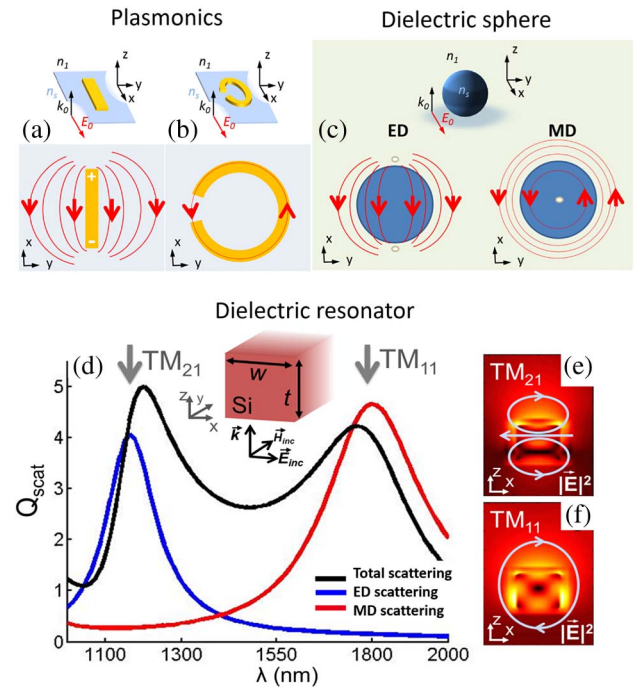

Fig. 3. Schematic representations of the electric fields in (a, b) plasmonic resonators and in (c) a dielectric sphere. Plasmonic rod antennas support only electric resonances with negligible magnetic contribution. Strong magnetic dipole resonance can be achieved in plasmonic particles by shaping the metallic rod in the form of a split ring resonator [71]. (d) Rectangular dielectric nanoparticles also exhibit electric and magnetic polarizabilities. Shown are the electric dipole (ED), magnetic dipole (MD), and total scattering cross sections (arbitrary units) associated with the corresponding modes shown in (e) and (f) [72].
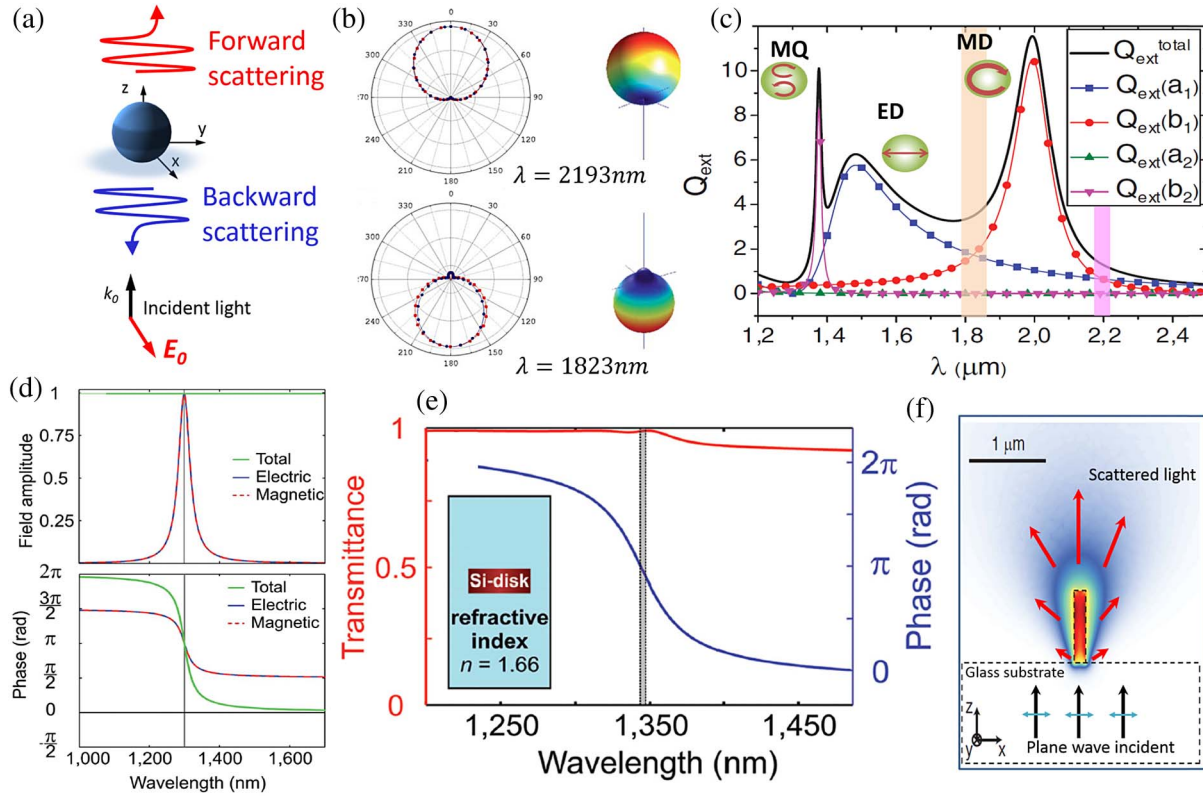
Fig. 4.   (a) Schematic representations of forward and backward scattering properties of a submicrometer dielectric particle. (b) Scattering diagrams for a 240 nm germanium sphere; the refractive index $n_{sp} = 4$ is constant and real in this wavelength range. Both polarizations, with the incident electric field parallel (TM or p polarization) or normal (TE or s polarization) to the plane of incidence are considered. (c) The total extinction cross section Q_{ext} (black solid line) versus wavelength depends on the contribution of each term in the Mie expansion. The red line corresponds to the magnetic dipole contribution, the blue curve to the electric dipole contribution, and the pink around 1.4 μm is attributed to the magnetic quadrupole. Forward/backward scattering is obtained when the electric and magnetic dipole resonances overlap in-phase/phase-opposition as denoted by the pink/orange highlighted region in the diagram around 1.8 μm/2.2 μm. The scattering diagrams presented in (b) correspond to these regions. (d) Amplitude and phase of the scattered field as functions of the wavelength of an idealized subwavelength array of loss-less nanodisks with electric and magnetic dipole resonances of equal strength and width under plane-wave illumination. (e) Numerically calculated transmittance intensity (red solid line) and phase (blue line) for an array of silicon nanoposts (radius = 242 nm, height = 220 nm) embedded in a homogeneous medium with optimized refractive index ($n = 1.66$). Resonance occurs at a design wavelength of ~1340 nm. Note the 2π phase coverage. (f) Schematic illustration superimposed with the finite elements simulation results of near-field distribution of light scattered by a single 715 nm tall circular amorphous silicon nanopost with a diameter of 150 nm in air. (b, c) are adapted from [73]; (d, e) are adapted from [74]; and (f) is adapted from [75].

for 3D metamaterials [71], exhibit also a resonant oscillating (dipolar) magnetic field in the middle of the ring [Fig. 3(a)]. Magnetic dipole modes also occur in dielectric particles with non-spherical geometries.

Nano-structured materials, such as a single layer of cylindrical silicon resonators on a silicon-on-insulator substrate, possess peak reflectance over 99% in the short-wavelength IR region due to strong separation between electric and magnetic dipole resonances [79,80]. Strong magnetic activities have also been reported in cubic resonator metamaterial in the mid-IR for application as optical magnetic mirrors [81,82].

In rectangular resonators, for example, the resonant wavelength can be easily tuned by changing either the geometry or the size of the scatterer [see Fig. 3(d)]. The combination of the scattering properties of both electric and magnetic resonances are of great interest for the realization of efficient planar optical metasurfaces. To fully appreciate the potential of "electromagnetic" scatterers for metasurfaces, we review here the work of Kerker *et al.* [83]. In this seminal paper, the authors considered a dielectric sphere with equal values of the relative dielectric

constant and relative magnetic permeability, $\varepsilon = \mu$, and showed that it exhibits zero backscattering and no depolarization. For long considered a theoretical curiosity, particles with $\varepsilon = \mu$ feature equal electric (a_n) and magnetic (b_n) multipole coefficients such that light is scattered to destructively interfere in the backward direction. This effect is known as the first Kerker condition. Considering nanoparticles with relatively small size, of the order of the illuminating wavelength, Mie's coefficients predicting the scattered light are greatly simplified and only a few coefficients remain to characterize the scattered field. This means that nanoparticles can be treated as dipolar particles in the sense that only the dipolar terms contribute to the scattered field [73].

The first two coefficients of the Mie expansion can therefore be used to describe the electric and magnetic dipole polarizabilities:

$$\alpha_e = \frac{3i\varepsilon}{2\,k^3}a_1 \quad \text{and} \quad \alpha_m = \frac{3i}{2\,\mu k^3}b_1,$$

where $k = n_{sp}k_o$.

Interference between the electric and magnetic dipoles leads to a backscattering cross section given by

$$\sigma_s(\pi) = 4\pi k^4 (|\varepsilon^{-1}\alpha_e|^2 + |\mu\alpha_m|^2)[1 + \cos(\pi - \Delta\phi_\alpha)], \qquad \textbf{(7)}$$

which has a minimum when dipoles are oscillating in phase ($\Delta\phi_\alpha = 0$) with an overall pattern similar to that of a Huygens' source [84–86].

This first Kerker condition has been predicted and verified in microwaves [87] and also at optical frequencies using germanium [88], silicon [89–91], and gallium arsenide nanospheres [85]. Illustrations of forward and backward radiation are presented in Fig. 4(a). The scattering diagrams corresponding to forward and backward radiation are also presented in Fig. 4(b). Forward/backward scattering is obtained when the electric and magnetic dipole resonances overlap in-phase/phase-opposition as denoted by the pink/orange highlighted region in Fig. 4(c). In the spectral domain, the shapes of electric and magnetic dipole resonances are not necessarily identical and overlapping, and one has to identify the position of the Kerker frequencies where destructive interference between the scattered fields by the induced electric and magnetic dipoles in the particle results in minima in the backward scattering directions. Considering an idealized subwavelength array of loss-less nanodisks with electric and magnetic dipole resonances of equal strength and width, unity transmission can be achieved under plane-wave illumination [Fig. 4(c)]. This condition is fulfilled with an array of Si nanodisks embedded in a homogeneous medium with optimized refractive index [Fig. 4(d)]. It has been pointed out that the interesting consequences of this interference between the incoming field and the scattered fields generated by the induced electric and magnetic dipoles in dielectric particles should be the basis of sophisticated antenna arrangements to achieve directionality and other interesting scattering effects on demand [87]. One of the main application of these "Huygens' sources" is the development of unity transmission Huygens' surfaces that can provide controllable phase delay retardation over the entire 2π range [74,92]. Huygens' metasurfaces are planar arrays of spatially varying nanoparticles with varying phase response and designed with balanced electric and magnetic responses (meta Huygens' sources) to minimize the backward radiated power and achieve impedance matching.

Arrays of wavelength-tall nanoposts in Fig. 4(f) or dielectric ridge waveguides made of amorphous silicon have recently been proposed as phase shifting elements in which the required phase accumulation is achieved via propagation over a subwavelength distance to create efficient transmitting metasurfaces in the mid-IR [57] and at IR wavelengths [93]. These devices work by engineering the dispersive response of nanoridges, an approach closely related to the earlier work on high contrast gratings [7,6,8,28,29,94–97]. High contrast gratings are composed of nanostructured materials with an index of refraction larger than the index of the substrate or of the material covering the nanostructure. The structure's height is sufficiently large to accommodate internal multimode propagation but remains sufficiently narrow to prevent propagation of non-zero diffraction orders in free space [95]. Near-perfect reflector lenses, artificial cavities, and even vertical surface emitting lasers have been realized using this approach [20,31,58,93,98–].

3. METALENSES, META-HOLOGRAMS, AND PHASE PLATES

Lenses are ubiquitous parts of any imaging system. High-numerical-aperture (NA) lenses are required to provide high-quality and subwavelength imaging resolution. However, they are usually expensive and bulky. This motivates the development of high-efficiency planar lenses with high NA, particularly in the visible spectrum because of widespread applications in imaging, spectroscopy, and microscopy. The wavefront scattered by a planar lens based on a metasurface is given by the envelope of the secondary spherical waves originated from the optical elements with subwavelength separation. For a very dense distribution of the latter, the phase profile can be assumed continuous, resulting in a perfect spherical wavefront for normally incident light of wavelength λ when $\varphi(x, y)$ is of the form (hyperboloid) [20,32,106]:

$$\varphi(x, y) = -\frac{2\pi}{\lambda}\left(\sqrt{x^2 + y^2 + f^2} - f\right), \qquad \textbf{(8)}$$

where x, y are the coordinates of the phase-shifting elements of the metasurface, and f is the focal distance of the lens. Physically, as one can see from Eq. (8), the phase shift imparted by the metasurface at (x, y) compensates for the difference in propagation phase between the refracted ray originating at that point and the central ray, so that all rays converge to the focal point at distance f.

Although highly efficient planar lenses have been reported [57,58], their operational bandwidth is limited to the IR region. Development of high-performance planar lenses in the visible spectrum requires new material/fabrication processes. Recently, planar lenses based on high-quality titanium dioxide (TiO_2) grown by atomic layer deposition (ALD) have been demonstrated [60]. For a detailed study of the optical properties of TiO_2 ALD films and metasurfaces, see [107]. TiO_2 has a high refractive index, and negligible absorption across the visible range; ALD films made of this material have negligible surface roughness. These features make it possible to closely pack the TiO_2 nanostructures at subwavelength distances due to the large optical confinement. As a result of these characteristics, planar lenses based on this technology have high efficiency and their design wavelength can be tuned across the entire visible spectrum, with high NA.

Figures 5(a)–5(c) show the schematic of the transmissive planar lens that utilizes, as building blocks, TiO_2 nanofins on a glass substrate. A scanning electron micrograph of a portion of a fabricated TiO_2 metasurface is shown in Fig. 2(f), revealing the high quality of the fabrication. A maximum aspect ratio of 15 with very vertical sidewalls, close to 89°, is obtained using this fabrication technique. In the metalens, the required phase map [Eq. (8)] is implemented via the rotation of nanofins [62] based on the PB phase [25,26]. These nanofins are designed as half-wave plates using structural birefringence (the effective index is different for two orthogonal polarizations normal to the propagation direction), so that they switch the handedness of incident circularly polarized light and, in addition, introduce a geometric phase equal to twice the rotation angle, as discussed in [59,62]. In this way, the hyperboloidal phase map is realized for normal incidence. Three planar lenses were designed at wavelengths of 405, 532, and 660 nm. All three planar lenses have diameters of 240 μm and focal lengths of 90 μm, giving a NA = 0.8. Figure 5(d) shows the simulated efficiencies for these three design wavelengths. The performance of these planar lenses was characterized using a custom-built optical setup. The measured focusing
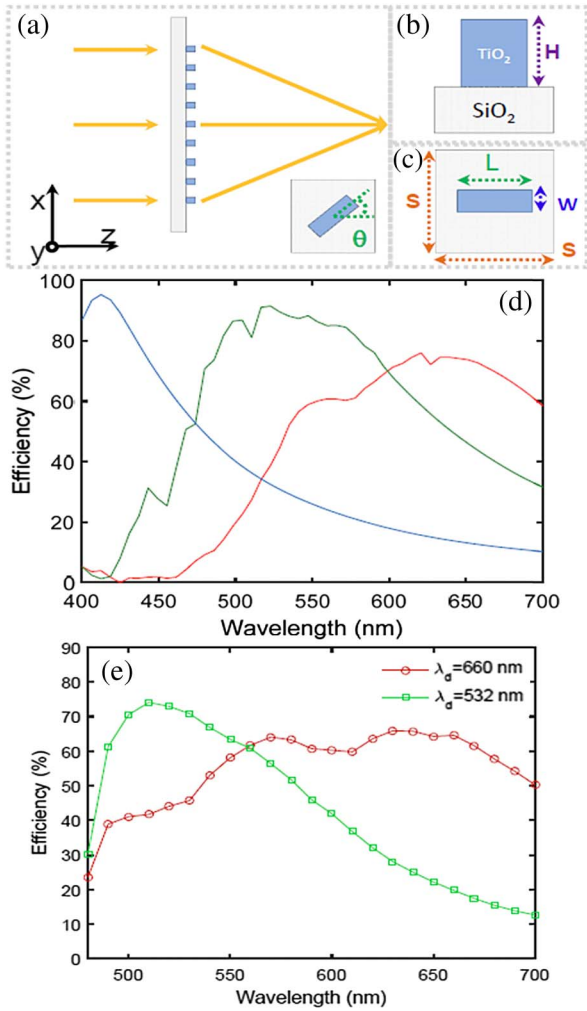
Fig. 5. (a) Schematic diagram of a transmissive planar lens. (b) Side view of TiO$_2$ nanofin on a glass substrate, showing its height. (c) Top view of the lens building block with dimensions $S \times S$ depicting nanofin width W and length L. (d) Simulation results showing the nanofin conversion efficiency that peaks at three design wavelengths of 405, 532, and 660 nm. (e) Measured focusing efficiency of the fabricated planar lenses designed at wavelengths of 660 and 532 nm. A scanning electron microscopy (SEM) image showing fabricated TiO$_2$ metasurfaces based on array of nanofins of 60×170 nm dimensions is presented in Fig 2(f). Figures are adapted from [60].

efficiencies of two planar lenses as a function of wavelength are shown in Fig. 5(e). For planar lenses designed at the wavelength 660 nm, the focusing efficiency peaks at 66% and remains above

50% over most of the visible spectrum. Planar lenses designed at wavelengths of 532 and 405 nm have measured peak efficiencies of 73% and 86%, respectively.

Figures 6(a)–6(c) show the measured focal spot profiles of planar lenses at their design wavelengths. Background-free and symmetric focal spots confirm the high quality of fabrication and the effectiveness of the phase realization mechanism. This is evident by comparing these focal spots with those of a state-of-the-art objective [60], which shows broader and non-symmetric intensity distributions. The measured full width at half-maximums (FWHMs) of the focal spots are 280, 375, and 450 nm for the planar lenses at their design wavelengths of 405, 532, and 660 nm, respectively. It is notable that these FWHM values are very close to the diffraction limit at the design wavelengths (FWHM $= \frac{\lambda_d}{2\text{NA}}$). Subwavelength resolution imaging was also demonstrated in this work. These planar lenses are not corrected for coma aberrations, so they have a limited field of view while being used for subwavelength imaging. Recently high-efficiency, high-NA (>0.85), diffraction-limited polarization insensitive metalenses have been demonstrated at visible wavelengths with performance comparable to lenses based on the geometric phase. These metalenses are made of TiO$_2$ cylindrical nanopillars of the same height but of varying diameter depending on their radial position, which controls the local phase shift [108]. Previously, polarization insensitive metalenses using SiN nanoposts were published with comparable NA with transmission efficiency of 35% and focusing efficiency of 10% in the visible regime [109]. HCG focusing plates with 0.7 NA have also been reported in the near-IR [110]. Recently, diffraction-limited mid-IR reflectarray lenses were demonstrated using metal–dielectric–metal structures consisting of Au disks on glass. Focusing efficiencies were near 80% [111]. High-efficiency transmissive dielectric metalenses in the mid-IR with 80% transmittance have been demonstrated [57] and 72% in the near-IR [93]. Diffraction-limited focusing and high efficiencies of these planar lenses together with their compact configuration make them widely applicable in laser-based spectroscopy, microscopy, and imaging. It is worth pointing out that recent components, such as Pendry lenses [112] and super-oscillatory lenses [113], have shown that one can obtain deep subwavelength focusing below the diffraction limit. However, the former method has strong limitations because any, even minimal, optical losses or/and very small imbalances between positive and negative optical space bring the lens back to the diffraction limit [114,115]. Concerning techniques using super-oscillations instead, there is a major loss in efficiency because of the high Fourier components used for focusing.
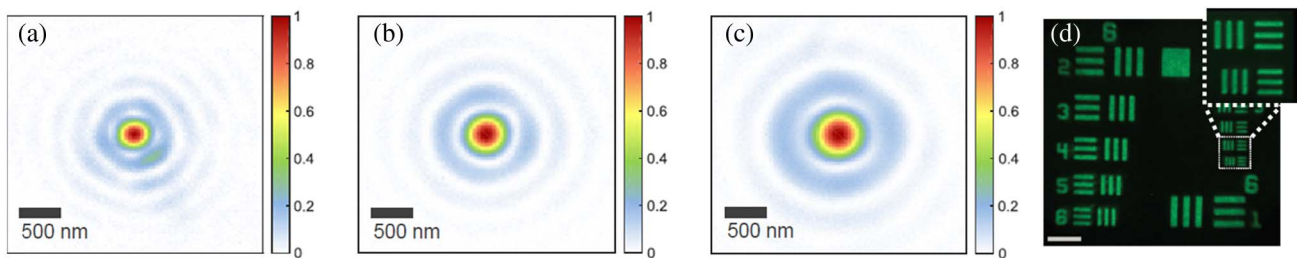

Fig. 6. Measured focal spot profiles of the planar lenses designed at wavelengths of (a) 405 nm, (b) 532 nm, and (c) 660 nm. (d) Imaging with a metalens designed at $\lambda = 532$ nm with diameter $D = 2$ mm and focal length $f = 0.725$ mm. Image of the 1951 USAF resolution test chart formed by the metalens. The laser wavelength is set at 530 nm. Scale bar, 40 µm. Figures are adapted from [60].
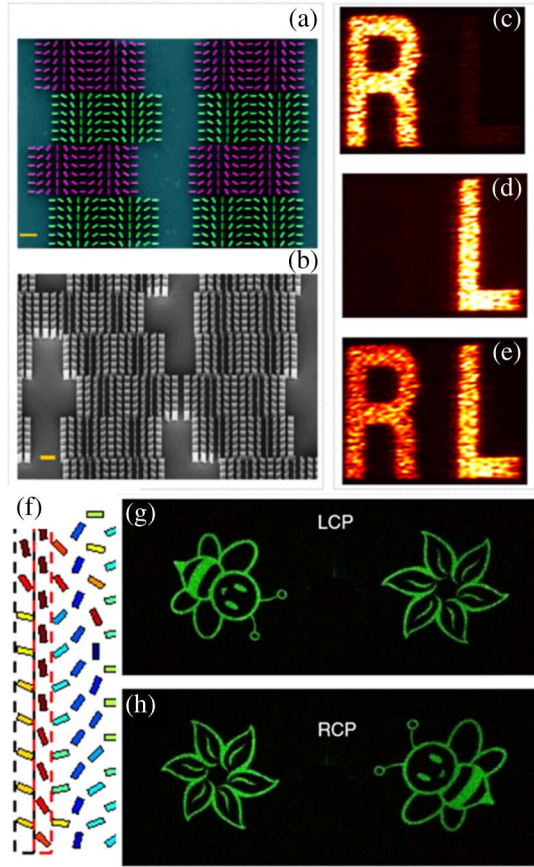
Fig. 7. (a) False color SEM image of four pixels of the chiral transmission dielectric hologram made of Si nanofins on glass. Each pixel consists of two parts: in purple, a meta-grating that imparts the required phase map for letter "L" and, in green, that for the phase map for letter "R." Nanofins have width $W = 85$ nm, length $L = 350$ nm, height $H = 1000$ nm, and center-to-center distance of 500 nm. Scale bar is 1 μm. (b) Side-view SEM image of a portion of the chiral hologram. Scale bar is 1 μm. (c)–(e) Holographic images formed in the first diffraction order (false colored) under different incident polarizations at wavelength $\lambda = 1350$ nm. The chiral hologram was illuminated by (c) right-circularly, (d) left-circularly, and (e) linearly polarized light, which result in the appearance of the letters "R," "L," and "RL," respectively. (f) Schematic of the nanorod distribution for the merged metasurface reflective hologram made of silver nanorods on glass with a silver back plane. The phase levels are denoted by the different colors of the nanorods. The nanorods in the columns with odd numbers and even numbers, starting from the left, contribute to the reconstruction of "bee" and "flower," respectively. (g) Experimentally obtained images for the incident light with left-circular (top) and right-circular (bottom) polarization. The wavelength of the incident light is 524 nm. Figures (a)–(e) are adapted from [116] and (f)–(h) from [105].

By engineering the response of phase shifting elements similar to the nanofins, it is possible to realize broadband and efficient meta-gratings [63]. These meta-gratings can serve as building blocks of holographic devices to accomplish chiral holograms [116]. In the fabricated device, each pixel is divided in two parts, half of it coupled to one handedness of the incident light and the other half to the opposite handedness [Figs. 7(a) and 7(b)]. These rotated nanofins introduce a geometrical phase like that in the case of planar lenses. In this way, the image displayed in the field of view of the optical system depends on the light handedness.

This device achieves broadband operation from the visible to the near-IR, and distortion-free performance and high efficiency in the near-IR. Figures 7(c)–7(e) show that a light intensity distribution corresponding to the letter "R" appears under right-circularly polarized illumination while it changes into the letter "L" for left-circular polarization. For linear polarization, both letters appear. In addition, this device demonstrates high values of absolute efficiency (up to 60%) and extinction ratio of up to 15 dB. A similar chiral holographic device concept based on the geometric phase was demonstrated in reflection using two spatially multiplexed arrays of silver nanoantennas on glass deposited on a silver film [Figs. 7(f)–7(h)] [105]. Form-birefringent computer-generated holograms have been fabricated previously using subwavelength binary gratings whose orientation controls the desired phase profile at mid- and near-IR frequencies [102]. A spatially varying transmittance phase, independent of the polarization of the incident beam, has been achieved using silicon metadevices at telecom wavelengths [117]. In this work, near-unity transmission efficiency and close to 2π phase coverage, enabled by utilizing the localized electric and magnetic Mie-type resonances of low-loss silicon nanoparticles, have been used to generate optical vortex beams [117]. High-efficiency vortex beam generation in reflection was reported also using the reflectarray design [19]. Highly efficient, sub–wavelength-thick, transmissive grating vortex plates to achieve polarization-independent operation have been demonstrated for the generation of high-order orbital angular momentum [110].

4. COMPENSATING WAVELENGTH-DEPENDENT PROPAGATION PHASE WITH METASURFACES

Recent works have reported metasurfaces with relatively broad reflectivity and transmission spectra [20,22,30,31,103–105] by designing resonators with broadband response, in order to achieve the high radiation losses necessary for high scattering efficiency. Absorption losses give a significantly smaller contribution to the spectral response. Because of this broadband response, the phase function implemented by the metasurface is relatively constant over a range of wavelengths. However, large chromatic aberrations are induced due to the dispersion of the phase accumulated by light during propagation, after the interaction with the metasurface [Fig. 8(a)]. This limitation can be overcome by compensating for the dispersion of the propagation phase with the wavelength-dependent phase shift imparted by the metasurface. In general, when light interacts with a metasurface, the total accumulated phase after the interface is the sum of two contributions:

$$\phi_{\text{tot}}(r, \lambda) = \phi_m(r, \lambda) + \phi_p(r, \lambda), \tag{9}$$

where ϕ_m is the phase shift imparted at point r by the metasurface and ϕ_p is the phase accumulated via propagation through free space. The first term is characterized by a large variation across the resonance, as discussed in the previous paragraphs. The second is given by $\phi_p(r, \lambda) = \frac{2\pi}{\lambda} l(r)$, where $l(r)$ is the physical distance between the interface at position r and the desired wavefront [Fig. 8(a)]. If one is able to maintain the condition of constructive interference at different wavelengths keeping ϕ_{tot} constant, the metasurface will function as an achromatic device. To do so, the dispersion of light has to be considered and compensated for the wavelengths of interest during the design of the metasurfaces. This approach has recently been proposed and
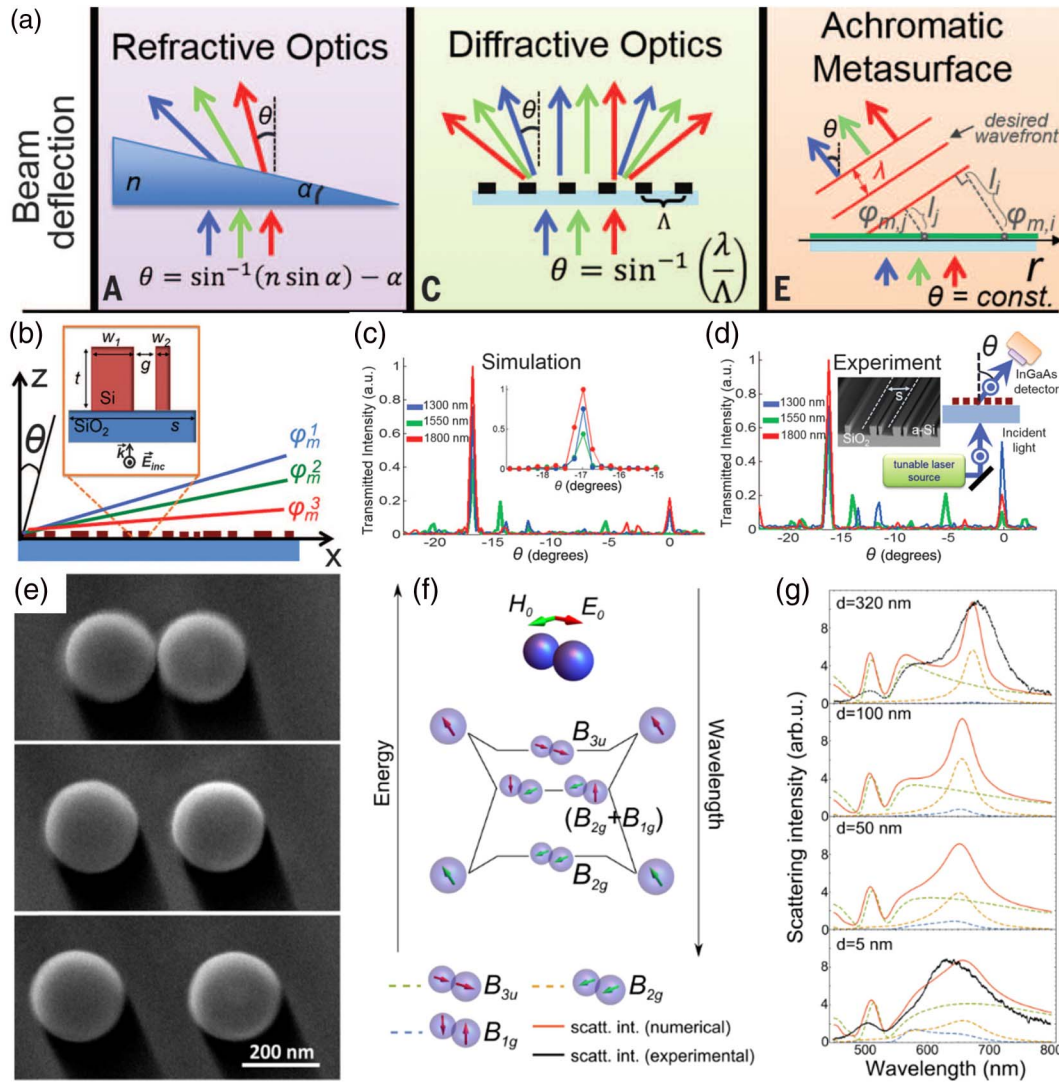
Fig. 8. (a) Refractive and diffractive optics are inherently dispersive, while metasurfaces can be designed to have an achromatic response. In the first two cases, the angles of deflection change as a function of wavelength. The achromatic metasurface consisting of subwavelength spaced resonators is designed to preserve its operation for multiple wavelengths. (b) Side view of the metasurface made of 240 unit cells, each consisting of a slot of the same width s, comprising two coupled rectangular dielectric resonators of fixed height t and varying widths w_1 and w_2 (inset). The metasurface is designed to diffract normally incident plane waves at three wavelengths ($\lambda_1 = 1300$ nm, $\lambda_2 = 1550$ nm, and $\lambda_3 = 1800$ nm) by the same angle ($\theta_0 = -17°$) by implementing a wavelength-dependent linear phase profile ϕ_m that compensates the wavelength-dependent propagation phase in air. (c) and (d) Numerical simulation and the experimental data of the far-field intensity distribution (normalized to the maximum value for each of the three wavelengths) as a function of the angle θ from the normal to the interface. (e) SEM images of Si nanoparticle dimer structures on a glass substrate. (f) Energy-level diagram describing the hybridization of electric (red arrows) and magnetic (green arrows) dipolar resonances of single scatterers. (g) Calculated scattering intensities of dimer structures (solid red line) for separations of $d = 320$, 100, 50, and 5 nm (top to bottom) compared to the experimental results (black line). The spectra are decomposed according to the hybridization scheme of electric and magnetic modes. Each single scatterer is an oblate ellipsoidal core(c-Si)–shell (SiO$_2$) structure with major and minor external radii of 95 and 78 nm, respectively, and a 4 nm oxide layer. Panels (a)–(d) are adapted from [72] and panels (e)–(g) are adapted from [118].

experimentally demonstrated in [72] using coupled rectangular dielectric resonators as multi-wavelength phase shifting building blocks. By placing two rectangular dielectric resonators in close proximity such that their near fields overlap, a system of coupled resonators is created. Near-field coupling influences the modal field distribution in the two neighboring resonators, which changes the spectral positions and widths of the resonances. The gap size and position can be utilized as additional degrees of freedom to engineer the scattering amplitude and phase. In

recent work, the hybridization of electric and magnetic dipolar modes has been studied, revealing that the contributions to the scattering arises from pairs of dipolar electric–electric and magnetic–magnetic modes (homogeneous modes), as well as from the mixed contribution of electric–magnetic modes (heterogeneous modes), induced due to the overlap between the electric and magnetic polarizabilities of single scatterers {Fig. 8(f) and [118]}. In this hybridization scheme, the two homogeneous modes denoted as B3u (so-called electric bonding mode,

reminiscent of that observed in numerous plasmonic systems) and B2g couple directly to the incident light, since they exhibit non-vanishing electric and magnetic dipolar modes, respectively. Similar to plasmonic dimers, the electric bonding mode redshifts with increasing separation, while the magnetic mode B2g [dashed orange line in Figs. 8(f) and 8(g)] blueshifts and deceases significantly in intensity. Two modes, referred to in terms of two heterogeneous modes each comprising an electric and a magnetic dipole mode, are excited indirectly by light coupling to the magnetic mode, which in turn induces the electric dipole in the resonators placed in close vicinity, blueshifting with decreasing separation. Near-field coupling, especially with multimode dielectric resonators, offers new degrees of freedom in controlling nanostructures' scattering properties and can be utilized to design complex systems. The presence of far-field-coupled heterogeneous modes and the low absorption losses in dielectrics are certainly advantageous compared to lossy plasmonic dimers and clusters. An example of an achromatic metasurface based on coupled resonant dielectrics is presented in Fig. 8(b). The achromatic metasurface works as a beam deflector based on dielectric resonators with a wavelength-independent angle of deflection for three discrete telecommunication wavelengths. The same approach has also been utilized to demonstrate achromatic lenses [119,120]. Designs of these achromatic devices based on coupled resonators or on meta-molecules is performed for specific, discrete, and predefined wavelengths. If light impinging on the device has a different wavelength than the designed values, typically between two designed wavelengths, the transmitted light generally exhibits a complex response, which often is not exploitable for a specific application. Broadband achromatic response can be achieved through compensation between the structure dispersion in nanoslit waveguides and the material dispersion [121]. It is clear from the introduction that metasurfaces and subwavelength gratings are intimately related, and one can approach this problem from the subwavelength grating concept, exploiting the inherent dispersion of propagation by diffracting light on graded dielectric interfaces made of grooves with spatially varying height. This idea has been presented in [122,123] and is illustrated in Fig. 9.

The design of such a grating interface requires optimizing the distribution of groove heights using a perturbation-based iterative method using a modified direct-binary-search (DBS) algorithm [122]. Interestingly, these diffractive devices can work on large bandwidth with super-achromatic performance over the continuous visible band with overall efficiency of around 10% [Fig. 9(d)]. The versatility in the choice of the wavelength-dependent phase in a single device allows also for functionalities that are very different (even opposite) from achromatic behavior. An optical device with enhanced dispersion or wavelength-dependent functionalities will find interesting applications in particular for ultra-compact spectrometry and nonlinear imaging technology.

5. CONCLUSIONS

During the past five years, metasurface technology has been developed at a frantic pace, going from inefficient chromatic devices working at long wavelengths—typically at mid-IR and terahertz frequencies—to high-NA components with subwavelength resolution and record high transmissivity in the visible. Achromatic devices and specific wavelength-dependent optical response can now be designed on demand on a single subwavelength-thick interface. Leveraging on various scattering mechanisms such as the PB phase, chirality, Kerker diffusion, and zero-order diffraction in a subwavelength grating, the concept of planar optics is currently transforming and modernizing photonics, establishing new functional devices for controlling, modulating, and steering light at optical frequencies. Modifying the reflection of light at arbitrary shaped metasurfaces leads to ultrathin cloaking sheets [124,125]. Whereas transformation optics determines bulk optical properties by exploiting the relationship between a given coordinate system and the coordinate system that conforms to the trajectory of light— i.e., the coordinate system is deformed to follow the light path [123,126–129], the concept of conformal boundary optics—a design theory that determines the optical response for designer input and output fields at arbitrarily shaped interfaces—discussed in [130] determines the optical properties of a metasurface of arbitrary geometry by exploiting the relationship between a given ambient coordinate system (chosen to decompose the electromagnetic field at each side of the boundary) and the coordinate system that follows the geometry of the boundary. The interface coordinate system is given by three components, two tangents, and one normal to the surface (see Fig. 10). Conformal boundary optics provides a wide range of new design opportunities, for example, to hide objects behind an optical curtain, to create optical illusions by reflecting virtual images, or to suppress the diffraction generally occurring during light scattering at corrugated interfaces.

Recent papers showed that it is in principle possible to experimentally realize a carpet cloak metasurface to hide an arbitrarily shaped object and to shape the wavefront of light at curved geometries [131,132]. Given the height of a 3D object with respect to a reference plane, the authors designed the interface phase response point-by-point to address wavefronts using pure phase functions, i.e., the amplitude is assumed uniform over the extent of the wavefront. In a recent paper, it is shown that it is not possible to funnel the incident wavefront into an arbitrary solution of choice if we are limited to using passive metasurfaces. Wave transformations over an ultrathin surface, even in their simplest form, e.g., for beam steering, inherently require the presence of
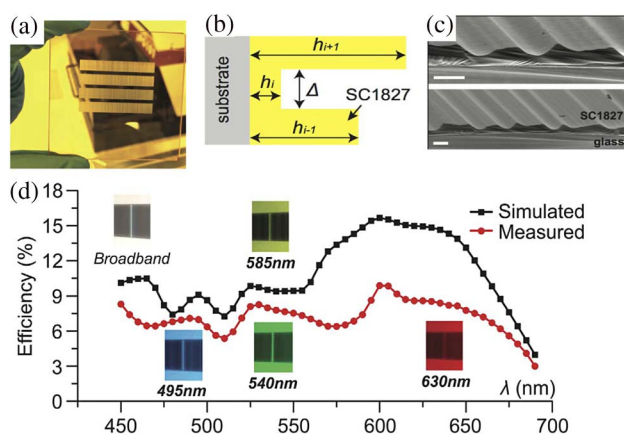

Fig. 9. (a) Photograph of four chromatic-aberration-corrected diffractive lenses (CACDLs) patterned on a glass substrate. (b) 1D CACDL is comprised of linear grooves with a designed height, h_i by a single step lithography on SC1827 photoresist. (c) SEM images of the cross sections of two CACDLs (scale bars: 5 μm). (d) Simulated (black) and measured (red) optical efficiency as a function of wavelength. Insets: photographs of the focus on a white observation screen at various wavelengths. The figure is adapted with permission from [122].
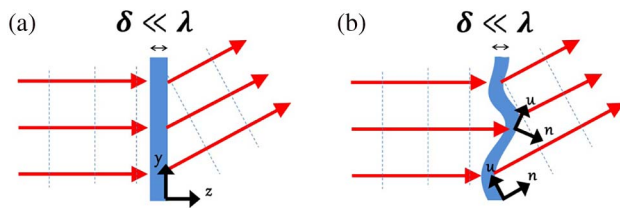
Fig. 10. (a) 2D planar metasurface of subwavelength thickness. For planar interfaces, generalized sheet boundary conditions readily apply, and the surface susceptibility tensors can be calculated. (b) The local coordinate system of the surface follows its local curvature, changing with the position along the interface. Boundary conditions of the fields are obtained in the coordinate system of the interface and are therefore position dependent. To produce an effect equivalent to that in (a), the surface susceptibilities of the optical interface have to be engineered to account for the effect of the physical distortion. The dashed blue lines denote the equiphase fronts of the electromagnetic fields. The figure is adapted with permission from [130].

balanced loss and gain to achieve unitary efficiency [132]. Addressing both problems of curvature and amplitude, the concept of conformal boundary optics goes beyond the pure local phase retardation. Interesting optical effects can be obtained using metasurfaces at the boundaries of metamaterials with arbitrary geometries [130]. For early works on coordinate transformation at interfaces see, for example, the formalism for the study of diffraction by a grating [133].

Though planar optics has the potential to displace conventional refractive optics in many applications, several challenges nevertheless remain, in particular in terms of theoretical modeling, design of building-block scattering elements, and large scale fabrication. First, metasurfaces are formally described using surface susceptibility/impedance/admittance tensors, where the latter are related through the generalized sheet transition conditions (GSTCs) to the incident, reflected, and transmitted fields on either side of the interface [134,135]. To exploit the full potential of these theoretical models, one needs additional tools that could directly connect shape and material properties of nanostructures to these complex macroscopic values.

Planar technology is the very essence of integrated circuit technology. To have a significant industrial impact, the manufacturing process of metasurfaces has to be compatible and tailored to proficiently use existing foundry technology (deep-UV steppers). This appears to be the case for metasurfaces based on ALD of TiO_2. New lithography techniques, in particular, nanoimprinting, roll-to-roll nanoimprinting, and soft lithography, can also address the problem of reproducible and large scale fabrication of metasurfaces.

This disruptive technology holds promise for major impact in many high-volume applications, such as novel camera modules for cell phones and laptops, wearable displays for augmented reality, metrology, 3D imaging, light concentration for solar cell panels and lasers [136], white lighting, laser-based microscopy, imaging, and spectroscopy. The new compact optical configuration will enable various innovative portable/handheld instruments for many applications.

REFERENCES

1. M. Born and E. Wolf, *Principles of Optics* (Pergamon, 1980).
2. D. Jackson, *Classical Electrodynamics*, 3rd ed. (Wiley, 1999).
3. W. E. Kock, "Metallic delay lenses," Bell Syst. Tech. J. **27**, 58–82 (1948).
4. W. Stork, N. Streibl, H. Haidner, and P. Kipfer, "Artificial distributed-index media fabricated by zero-order gratings," Opt. Lett. **16**, 1921 (1991).
5. M. W. Farn, "Binary gratings with increased efficiency," Appl. Opt. **31**, 4453–4458 (1992).
6. P. Lalanne, S. Astilean, P. Chavel, E. Cambril, and H. Launois, "Blazed binary subwavelength gratings with efficiencies larger than those of conventional échelette gratings," Opt. Lett **23**, 1081–1083 (1998).
7. P. Lalanne, "Waveguiding in blazed-binary diffractive elements," J. Opt. Soc. Am. A **16**, 2517–2520 (1999).
8. P. Lalanne, S. Astilean, P. Chavel, E. Cambril, and H. Launois, "Design and fabrication of blazed binary diffractive elements with sampling periods smaller than the structural cutoff," J. Opt. Soc. Am. A **16**, 1143–1156 (1999).
9. D. Berry, R. Malech, and W. Kennedy, "The reflectarray antenna," IEEE Trans. Antennas Propag. **11**, 645–651 (1963).
10. D. M. Pozar and T. A. Metzler, "Analysis of a reflectarray antenna using microstrip patches of variable size," Electron. Lett. **29**, 657–658 (1993).
11. J. Huang, *Reflectarray Antenna* (Wiley, 2005).
12. J. A. Encinar, "Design of two-layer printed reflectarrays using patches of variable size," IEEE Trans. Antennas Propag. **49**, 1403–1410 (2001).
13. N. Yu, P. Genevet, M. A. Kats, F. Aieta, J.-P. Tetienne, F. Capasso, and Z. Gaburro, "Light propagation with phase discontinuities: generalized laws of reflection and refraction," Science **334**, 333–337 (2011).
14. E. H. Khoo, E. P. Li, and K. B. Crozier, "Plasmonic wave plate based on subwavelength nanoslits," Opt. Lett. **36**, 2498–2500 (2011).
15. Y. Zhao and A. Alù, "Manipulating light polarization with ultrathin plasmonic metasurfaces," Phys. Rev. B **84**, 205428 (2011).
16. F. Aieta, P. Genevet, N. F. Yu, M. A. Kats, Z. Gaburro, and F. Capasso, "Out-of-plane reflection and refraction of light by anisotropic optical antenna metasurfaces with phase discontinuities," Nano Lett. **12**, 1702–1706 (2012).
17. P. Genevet, N. Yu, F. Aieta, J. Lin, M. A. Kats, R. Blanchard, M. O. Scully, Z. Gaburro, and F. Capasso, "Ultra-thin plasmonic optical vortex plate based on phase discontinuities," Appl. Phys. Lett. **100**, 013101 (2012).
18. E. Karimi, S. A. Schulz, I. De Leon, H. Qassim, J. Upham, and R. W. Boyd, "Generating optical orbital angular momentum at visible wavelengths using a plasmonic metasurface," Light Sci. Appl. **3**, E167 (2014).
19. Y. Yang, W. Wang, P. Moitra, I. I. Kravchenko, D. P. Briggs, and J. Valentine, "Dielectric meta-reflectarray for broadband linear polarization conversion and optical vortex generation," Nano Lett. **14**, 1394–1399 (2014).
20. A. Pors, M. G. Nielsen, R. L. Eriksen, and S. I. Bozhevolnyi, "Broadband focusing flat mirrors based on plasmonic gradient metasurfaces," Nano Lett. **13**, 829–834 (2013).
21. A. V. Kildishev, A. Boltasseva, and V. M. Shalaev, "Planar photonics with metasurfaces," Science **339**, 1232009 (2013).
22. N. Yu, P. Genevet, F. Aieta, M. Kats, R. Blanchard, G. Aoust, J.-P. Tetienne, Z. Gaburro, and F. Capasso, "Flat optics: controlling wavefronts with optical antenna metasurfaces," IEEE J. Sel. Top. Quantum Electron. **19**, 4700423 (2013).
23. H. Liu, M. Q. Mehmood, K. Huang, L. Ke, H. Ye, P. Genevet, M. Zhang, A. Danner, S. P. Yeo, C.-W. Qiu, and J. Teng, "Twisted focusing of optical vortices with broadband flat spiral zone plates," Adv. Opt. Mater. **2**, 1193–1198 (2014).
24. M. A. Kats, P. Genevet, G. Aoust, N. Yu, R. Blanchard, F. Aieta, Z. Gaburro, and F. Capasso, "Giant birefringence in optical antenna arrays with widely tailorable optical anisotropy," Proc. Natl. Acad. Sci. USA **109**, 12364–12368 (2012).

25. M. V. Berry, "The adiabatic phase and Pancharatnam's phase for polarized light," J. Mod. Opt. **34**, 1401–1407 (1987).

26. S. Pancharatnam, "Generalized theory of interference, and its applications," Proc. Indian Acad. Sci. A **44**, 247–262 (1956).

27. A. Niv, G. Biener, V. Kleiner, and E. Hasman, "Propagation-invariant vectorial Bessel beams obtained by use of quantized Pancharatnam-Berry phase optical elements," Opt. Lett. **29**, 238–240 (2004).

28. G. Biener, A. Niv, V. Kleiner, and E. Hasman, "Formation of helical beams by use of Pancharatnam-Berry phase optical elements," Opt. Lett. **27**, 1875–1877 (2002).

29. Z. Bomzon, G. Biener, V. Kleiner, and E. Hasman, "Space-variant Pancharatnam–Berry phase optical elements with computer-generated subwavelength gratings," Opt. Lett. **27**, 1141–1143 (2002).

30. X. Ni, N. K. Emani, A. V. Kildishev, A. Boltasseva, and V. M. Shalaev, "Broadband light bending with plasmonic nanoantennas," Science **335**, 427 (2012).

31. S. Sun, K.-Y. Yang, C.-M. Wang, T.-K. Juan, W. T. Chen, C. Y. Liao, Q. He, S. Xiao, W.-T. Kung, G.-Y. Guo, L. Zhou, and D. P. Tsai, "High-efficiency broadband anomalous reflection by gradient metasurfaces," Nano Lett. **12**, 6223–6229 (2012).

32. F. Aieta, P. Genevet, M. A. Kats, N. Yu, R. Blanchard, Z. Gaburro, and F. Capasso, "Aberration-free ultrathin flat lenses and axicons at telecom wavelengths based on plasmonic metasurfaces," Nano Lett. **12**, 4932–4936 (2012).

33. B. Desiatov, N. Mazurski, Y. Fainman, and U. Levy, "Polarization selective beam shaping using nanoscale dielectric metasurfaces," Opt. Express **23**, 22611–22618 (2015).

34. X. Chen, L. Huang, H. Mühlenbernd, G. Li, B. Bai, Q. Tan, G. Jin, C.-W. Qiu, S. Zhang, and T. Zentgraf, "Dual-polarity plasmonic metalens for visible light," Nat. Commun. **3**, 1198 (2012).

35. X. Yin, Z. Ye, J. Rho, Y. Wang, and X. Zhang, "Photonic spin Hall effect at metasurfaces," Science **339**, 1405–1407 (2013).

36. N. Shitrit, I. Yulevich, E. Maguid, D. Ozeri, D. Veksler, V. Kleiner, and E. Hasman, "Spin-optical metamaterial route to spin-controlled photonics," Science **340**, 724–726 (2013).

37. X. H. Ling, X. X. Zhou, W. X. Shu, H. L. Luo, and S. C. Wen, "Realization of tunable photonic spin Hall effect by tailoring the Pancharatnam-Berry phase," Sci. Rep. **4**, 5557 (2014).

38. X. Ling, X. Zhou, X. Yi, W. Shu, Y. Liu, S. Chen, H. Luo, S. Wen, and D. Fan, "Giant photonic spin Hall effect in momentum space in a structured metamaterial with spatially varying birefringence," Light Sci. Appl. **4**, E290 (2015).

39. X. J. Ni, A. V. Kildishev, and V. M. Shalaev, "Metasurface holograms for visible light," Nat. Commun. **4**, 2807 (2013).

40. L. L. Huang, X. Z. Chen, H. Mühlenbernd, H. Zhang, and S. M. Chen, "Three-dimensional optical holography using a plasmonic metasurface," Nat. Commun. **4**, 2808 (2013).

41. P. Genevet and F. Capasso, "Holographic optical metasurfaces: a review of current progress," Rep. Prog. Phys. **78**, 024401 (2015).

42. J. Arnaud and F. Pelow, "Resonant-grid quasi-optical diplexers," Bell Syst. Tech. J. **54**, 263–283 (1975).

43. D. M. Pozar, S. D. Targonski, and H. D. Syrigos, "Design of millimeter wave microstrip reflectarrays," IEEE Trans. Antennas Propag. **45**, 287–296 (1997).

44. C. G. M. Ryan, M. Z. Chaharmir, J. Shaker, J. R. Bray, Y. M. M. Antar, and A. Ittipiboon, "A wideband transmitarray using dual-resonant double square rings," IEEE Trans. Antennas Propag. **58**, 1486–1493 (2010).

45. P. Padilla, A. Muñoz-Acevedo, M. Sierra-Castaner, and M. Sierra-Perez, "Electronically reconfigurable transmitarray at Ku band for microwave applications," IEEE Trans. Antennas Propag. **58**, 2571–2579 (2010).

46. N. Liu, M. Mesch, T. Weiss, M. Hentschel, and H. Giessen, "Infrared perfect absorber and its application as plasmonic sensor," Nano Lett. **10**, 2342–2348 (2010).

47. A. P. Feresidis, G. Goussetis, S. Wang, and J. C. Vardaxoglou, "Artificial magnetic conductor surfaces and their application to low-profile high-gain planar antennas," IEEE Trans. Antennas Propag. **53**, 209–215 (2005).

48. S. B. Glybovski, S. A. Tretyakov, P. A. Belov, Y. S. Kivshar, and C. R. Simovski, "Metasurfaces: from microwaves to visible," Phys. Rep. **634**, 1–72 (2016).

49. A. Y. Zhu, A. I. Kuznetsov, B. Luk'yanchuk, N. Engheta, and P. Genevet, "Traditional and emerging materials for optical metasurfaces," Nanophotonics (2016), doi:10.1515/nanoph-2016-0032.

50. N. Yu and F. Capasso, "Flat optics with designer metasurfaces," Nat. Mater. **13**, 139–150 (2014).

51. C. Huygens, *Traite De La Lumiere* (Van Der Aa, 1690).

52. A. Grbic and C. Pfeiffer, "Metamaterial Huygens' surfaces: tailoring wave fronts with reflectionless sheets," Phys. Rev. Lett. **110**, 197401 (2013).

53. S. Larouche and D. R. Smith, "Reconciliation of generalized refraction with diffraction theory," Opt. Lett. **37**, 2391–2393 (2012).

54. R. W. P. King, *The Theory of Linear Antennas* (Harvard University, 1956).

55. M. A. Kats, N. Yu, P. Genevet, Z. Gaburro, and F. Capasso, "Effect of radiation damping on the spectral response of plasmonic components," Opt. Express **19**, 21748–21753 (2011).

56. W. Luo, S. Xiao, Q. He, S. Sun, and L. Zhou, "Photonic spin Hall effect with nearly 100% efficiency," Adv. Opt. Mater. **3**, 1102–1108 (2015).

57. A. Arbabi, R. M. Briggs, Y. Horie, M. Bagheri, and A. Faraon, "Efficient dielectric metasurface collimating lenses for mid-infrared quantum cascade lasers," Opt. Express **23**, 33310–33317 (2015).

58. C. F. R. Mateus, M. C. Y. Huang, L. Chen, C. J. Chang-Hasnain, and Y. Suzuki, "Broad-band mirror (1.12–1.62 μm) using a subwavelength grating," IEEE Photon. Technol. Lett. **16**, 1676–1678 (2004).

59. G. Zheng, H. Mühlenbernd, M. Kenney, G. Li, T. Zentgraf, and S. Zhang, "Metasurface holograms reaching 80% efficiency," Nat. Nanotechnol. **10**, 308–312 (2015).

60. M. Khorasaninejad, W. T. Chen, R. C. Devlin, J. Oh, A. Y. Zhu, and F. Capasso, "Metalenses at visible wavelengths: diffraction-limited focusing and subwavelength resolution imaging," Science **352**, 1190–1194 (2016).

61. D. Lin, P. Fan, E. Hasman, and M. Brongersma, "Dielectric gradient metasurface optical elements," Science **345**, 298–302 (2014).

62. K. B. Crozier and M. Khorasaninejad, "Silicon nanofin grating as a miniature chirality-distinguishing beam-splitter," Nat. Commun. **5**, 5386 (2014).

63. M. Khorasaninejad and F. Capasso, "Broadband multifunctional efficient meta-gratings based on dielectric waveguide phase shifters," Nano Lett. **15**, 6709–6715 (2015).

64. M. Al-Joumayly and N. Behdad, "A generalized method for synthesizing low-profile, band-pass frequency selective surfaces with non-resonant constituting elements," IEEE Trans. Antennas Propag. **58**, 4033–4041 (2010).

65. D. Pozar, "Flat lens antenna concept using aperture coupled microstrip patches," Electron. Lett. **32**, 2109–2111 (1996).

66. K. Sarabandi and N. Behdad, "A frequency selective surface with miniaturized elements," IEEE Trans. Antennas Propag. **55**, 1239–1245 (2007).

67. C. Ryan, M. Chaharmir, J. Shaker, J. Bray, Y. Antar, and A. Ittipiboon, "A wideband transmitarray using dual-resonant double square rings," IEEE Trans. Antennas Propag. **58**, 1486–1493 (2010).

68. B. Memarzadeh and H. Mosallaei, "Array of planar plasmonic scatterers functioning as light concentrator," Opt. Lett. **36**, 2569–2571 (2011).

69. M. Faraday, "Experimental relations of gold (and other metals) to light," Philos. Trans. R. Soc. London **147**, 145–181 (1857).

70. G. Mie, "Beiträge zur optik trüber medien, speziell kolloidaler metallösungen," Ann. Phys. **330**, 377–445 (1908).

71. L. A. Whitehead and W. N. Hardy, "Split-ring resonator for use in magnetic resonance from 200-2000," Rev. Sci. Instrum. **52**, 213–216 (1981).

72. F. Aieta, M. A. Kats, P. Genevet, and F. Capasso, "Multiwavelength achromatic metasurfaces by dispersive phase compensation," Science **347**, 1342–1345 (2015).

73. R. Gomez-Medina, B. García-Cámara, I. Suárez-Lacalle, F. González, F. Moreno, M. Nieto-Vesperinas, and J. José Sáenz, "Electric and magnetic dipolar response of germanium nanospheres: interference effects, scattering anisotropy, and optical forces," J. Nanophotonics **5**, 053512 (2011).

74. M. Decker, I. Staude, M. Falkner, J. Dominguez, D. N. Neshev, I. Brener, T. Pertsch, and Y. S. Kivshar, "High-efficiency dielectric Huygens' surfaces," Adv. Opt. Mater. **3**, 813–820 (2015).

75. A. Arbabi, Y. Horie, M. Bagheri, and A. Faraon, "Dielectric metasurfaces for complete control of phase and polarization with subwavelength

spatial resolution and high transmission," Nat. Nanotechnol. **10**, 937–943 (2015).

76. J. A. Schuller, R. Zia, T. Taubner, and M. L. Brongersma, "Dielectric metamaterials based on electric and magnetic resonances of silicon carbide particles," Phys. Rev. Lett. **99**, 107401 (2007).

77. A. B. Evlyukhin, S. M. Novikov, U. Zywietz, R. L. Eriksen, C. Reinhardt, and S. I. Bozhevolnyi, "Chichkov demonstration of magnetic dipole resonances of dielectric nanospheres in the visible region," Nano Lett. **12**, 3749–3755 (2012).

78. A. I. Kuznetsov, A. E. Miroshnichenko, Y. H. Fu, J. Zhang, and B. Luk'yanchuk, "Magnetic light," Sci. Rep. **2**, 492 (2012).

79. P. Moitra, B. A. Slovick, Z. G. Yu, S. Krishnamurthy, and J. Valentine, "Experimental demonstration of a broadband all-dielectric metamaterial perfect reflector," Appl. Phys. Lett. **104**, 171102 (2014).

80. P. Moitra, B. A. Slovick, W. Li, I. I. Kravchenko, D. P. Briggs, S. Krishnamurthy, and J. Valentine, "Large-scale all-dielectric metamaterial perfect reflectors," ACS Photon. **2**, 692–698 (2015).

81. J. C. Ginn, I. Brener, D. W. Peters, J. R. Wendt, J. O. Stevens, P. F. Hines, L. I. Basilio, L. K. Warne, J. F. Ihlefeld, P. G. Clem, and M. B. Sinclair, "Realizing optical magnetism from dielectric metamaterials," Phys. Rev. Lett. **108**, 097402 (2012).

82. S. Liu, M. B. Sinclair, T. S. Mahony, Y. C. Jun, S. Campione, J. Ginn, D. A. Bender, J. R. Wendt, J. F. Ihlefeld, P. G. Clem, J. B. Wright, and I. Brener, "Optical magnetic mirrors without metals," Optica **1**, 250–256 (2014).

83. M. Kerker, D.-S. Wang, and C. L. Giles, "Electromagnetic scattering by magnetic spheres," J. Opt. Soc. Am. **73**, 765–767 (1983).

84. M. Nieto-Vesperinas, R. Gomez-Medina, and J. J. Saenz, "Angle-suppressed scattering and optical forces on submicrometer dielectric particles," J. Opt. Soc. Am. A **28**, 54–60 (2011).

85. S. Person, M. Jain, Z. Lapin, J. J. Sáenz, G. Wicks, and L. Novotny, "Demonstration of zero optical backscattering from single nanoparticles," Nano Lett. **13**, 1806–1809 (2013).

86. B. Rolly, B. Stout, and N. Bonod, "Boosting the directivity of optical antennas with magnetic and electric dipolar resonant particles," Opt. Express **20**, 20376–20386 (2012).

87. J. M. Geffrin, B. García-Cámara, R. Gómez-Medina, P. Albella, L. Froufe-Pérez, C. Eyraud, A. Litman, R. Vaillon, F. González, and M. Nieto-Vesperinas, "Magnetic and electric coherence in forward-and back-scattered electromagnetic waves by a single dielectric subwavelength sphere," Nat. Commun. **3**, 1171 (2012).

88. L. Cao, J. S. White, J. S. Park, J. A. Schuller, B. M. Clemens, and M. L. Brongersma, "Engineering light absorption in semiconductor nanowire devices," Nat. Mater. **8**, 643–647 (2009).

89. L. Cao, P. Fan, E. S. Barnard, A. M. Brown, and M. L. Brongersma, "Tuning the color of silicon nanostructures," Nano Lett. **10**, 2649–2654 (2010).

90. Y. H. Fu, A. I. Kuznetsov, A. E. Miroshnichenko, Y. F. Yu, and B. Luk'yanchuk, "Directional visible light scattering by silicon nanoparticles," Nat. Commun. **4**, 1527 (2013).

91. A. B. Evlyukhin, R. L. Eriksen, W. Cheng, J. Beermann, C. Reinhardt, A. Petrov, S. Prorok, M. Eich, B. N. Chichkov, and S. I. Bozhevolnyi, "Optical spectroscopy of single Si nanocylinders with magnetic and electric resonances," Sci. Rep. **4**, 4126 (2014).

92. Y. F. Yu, A. Y. Zhu, R. Paniagua-Dominguez, Y. H. Fu, B. Luk'yanchuk, and A. I. Kuznetsov, "High-transmission dielectric metasurface with 2π phase control at visible wavelengths," Adv. Opt. Mater. **3**, 813–820 (2015).

93. A. Arbabi, Y. Horie, A. J. Ball, M. Bagheri, and A. Faraon, "Subwavelength-thick lenses with high numerical apertures and large efficiency based on high-contrast transmitarrays," Nat. Commun. **6**, 7069 (2015).

94. T. K. Gaylord and M. G. Moharam, "Rigorous coupled-wave analysis of planar-grating diffraction," J. Opt. Soc. Am. **71**, 811–818 (1981).

95. P. Lalanne, J. P. Hugonin, and P. Chavel, "Optical properties of deep lamellar gratings: a coupled Bloch-mode insight," J. Lightwave Technol. **24**, 2442–2449 (2006).

96. C. J. Chang-Hasnain and W. Yang, "High-contrast gratings for integrated optoelectronics," Adv. Opt. Photon. **4**, 379–440 (2012).

97. S. Collin, "Nanostructure arrays in free-space: optical properties and applications," Rep. Prog. Phys. **77**, 126402 (2014).

98. C. Mateus, M. Huang, Y. Deng, A. Neureuther, and C. Chang-Hasnain, "Ultrabroadband mirror using low-index cladded subwavelength grating," IEEE Photon. Technol. Lett. **16**, 518–520 (2004).

99. D. Fattal, J. Li, Z. Peng, M. Fiorentino, and R. G. Beausoleil, "Flat dielectric grating reflectors with focusing abilities," Nat. Photonics **4**, 466–470 (2010).

100. M. C. Y. Huang, Y. Zhou, and C. J. Chang-Hasnain, "A surface-emitting laser incorporating a high-index-contrast subwavelength grating," Nat. Photonics **1**, 119–122 (2007).

101. J. Li, D. Fattal, M. Fiorentino, and R. G. Beausoleil, "Strong optical confinement between nonperiodic flat dielectric gratings," Phys. Rev. Lett. **106**, 193901 (2011).

102. U. Levy, H.-C. Kim, C.-H. Tsai, and Y. Fainman, "Near-infrared demonstration of computer-generated holograms implemented by using subwavelength gratings with space-variant orientation," Opt. Lett. **30**, 2089–2091 (2005).

103. W. T. Chen, K.-Y. Yang, C.-M. Wang, Y.-W. Huang, G. Sun, I.-D. Chiang, C. Y. Liao, W.-L. Hsu, H. T. Lin, S. Sun, L. Zhou, A. Q. Liu, and D. P. Tsai, "High-efficiency broadband meta-hologram with polarization- controlled dual images," Nano Lett. **14**, 225–230 (2014).

104. J. Lin, P. Genevet, M. A. Kats, N. Antoniou, and F. Capasso, "Nanostructured holograms for broadband manipulation of vector beams," Nano Lett. **13**, 4269–4274 (2013).

105. D. Wen, F. Yue, G. Li, G. Zheng, K. Chan, S. Chen, M. Chen, K. F. Li, P. W. H. Wong, K. W. Cheah, E. Y. B. Pun, S. Zhang, and X. Chen, "Helicity multiplexed broadband metasurface holograms," Nat. Commun. **6**, 8241 (2015).

106. F. Aieta, P. Genevet, M. Kats, and F. Capasso, "Aberrations of flat lenses and aplanatic metasurfaces," Opt. Express **21**, 31530–31539 (2013).

107. R. C. Devlin, M. Khorasaninejad, W.-T. Chen, J. Oh, and F. Capasso, "Broadband high efficiency dielectric metasurfaces at visible wavelengths," Proc. Natl. Acad. Sci. USA **113**, 10473–10478 (2016).

108. M. Khorasaninejad, A. Zhu, C. Roques-Carmes, W. T. Chen, J. Oh, I. Mishra, R. C. Devlin, and F. Capasso, "Polarization-insensitive metalenses at visible wavelengths," Nano Lett. **16**, 7229–7234 (2016).

109. A. Zhan, S. Colburn, R. Trivedi, T. K. Fryett, C. M. Dodson, and A. Majumdar, "Low-contrast dielectric metasurface optics," ACS Photon. **3**, 209–214 (2016).

110. S. Vo, D. Fattal, W. V. Sorin, Z. Peng, T. Tran, M. Fiorentino, and R. G. Beausoleil, "Sub-wavelength grating lenses with a twist," IEEE Photon. Technol. Lett. **26**, 1375–1378 (2014).

111. S. Zhang, M.-H. Kim, F. Aieta, A. She, T. Mansuripur, I. Gabay, M. Khorasaninejad, D. Rousso, X. Wang, M. Troccoli, N. Yu, and F. Capasso, "High efficiency near diffraction-limited mid-infrared flat lenses based on metasurface reflectarrays," Opt. Express **24**, 18024–18034 (2016).

112. J. B. Pendry, "Negative refraction makes a perfect lens," Phys. Rev. Lett. **85**, 3966–3969 (2000).

113. N. I. Zheludev and T. F. Rogers, "Optical super-oscillations: subwavelength light focusing and super-resolution imaging," J. Opt. **15**, 094008 (2013).

114. E. E. Narimanov and V. A. Podolskiy, "Near-sighted superlens," Opt. Lett. **30**, 75–77 (2005).

115. R. Merlin, "Analytical solution of the almost-perfect-lens problem," Appl. Phys. Lett. **84**, 1290–1292 (2004).

116. M. Khorasaninejad, A. Ambrosio, P. Kanhaiya, and F. Capasso, "Broadband and chiral binary dielectric meta-holograms," Sci. Adv. **2**, e1501258 (2016).

117. K. E. Chong, I. Staude, A. James, J. Dominguez, S. Liu, S. Campione, G. S. Subramania, T. S. Luk, M. Decker, D. N. Neshev, I. Brener, and Y. S. Kivshar, "Polarization-independent silicon metadevices for efficient optical wavefront control," Nano Lett. **15**, 5369–5374 (2015).

118. U. Zywietz, M. K. Schmidt, A. B. Evlyukhin, C. Reinhardt, J. Aizpurua, and B. N. Chichkov, "Electromagnetic resonances of silicon nanoparticle dimers in the visible," ACS Photon. **2**, 913–920 (2015).

119. M. Khorasaninejad, F. Aieta, P. Kanhaiya, M. A. Kats, P. Genevet, D. Rousso, and F. Capasso, "Achromatic metasurface lens at telecommunication wavelengths," Nano Lett. **15**, 5358–5362 (2015).

120. E. Arbabi, A. Arbabi, S. M. Kamali, Y. Horie, and A. Faraon, "Multiwavelength polarization-insensitive lenses based on dielectric metasurfaces with meta-molecules," Optica **3**, 628 (2016).

121. Y. Li, X. Li, M. Pu, Z. Zhao, X. Ma, Y. Wang, and X. Luo, "Achromatic flat optical components via compensation between structure and material dispersions," Sci. Rep. **6**, 19885 (2016).

122. P. Wang, N. Mohammad, and R. Menon, "Chromatic-aberration-corrected diffractive lenses for ultra-broadband focusing," Sci. Rep. **6**, 21545 (2016).

123. J. B. Pendry, D. Schurig, and D. R. Smith, "Controlling electromagnetic fields," Science **312**, 1780–1782 (2006).

124. P.-Y. Chen and A. Alù, "Mantle cloaking using thin patterned metasurfaces," Phys. Rev. B **84**, 205110 (2011).

125. N. Xi, Z. J. Wong, M. Mrejen, Y. Wang, and X. Zhang, "An ultrathin invisibility skin cloak for visible light," Science **349**, 1310–1314 (2015).

126. U. Leonhardt, "Optical conformal mapping," Science **312**, 1777–1780 (2006).

127. L. Xu and H. Chen, "Conformal transformation optics," Nat. Photonics **9**, 15–23 (2014).

128. A. J. Ward and J. B. Pendry, "Refraction and geometry in Maxwell's equations," J. Mod. Opt. **43**, 773–793 (1996).

129. U. Leonhardt and T. G. Philbin, "Transformation optics and the geometry of light," Prog. Opt. **53**, 69–152 (2009).

130. J. Y. H. Teo, L. J. Wong, C. Molardi, and P. Genevet, "Controlling electromagnetic fields at boundaries of arbitrary geometries," Phys. Rev. A **94**, 013824 (2016).

131. S. M. Kamali, A. Arbabi, E. Arbabi, Y. Horie, and A. Faraon, "Decoupling optical function and geometrical form using conformal flexible dielectric metasurfaces," Nat. Commun. **7**, 11618 (2016).

132. N. M. Estakhri and A. Alù, "Wave-front transformation with gradient metasurfaces," Phys. Rev. X **6**, 041008 (2016).

133. J. Chandezon, G. Raoult, and D. Maystre, "A new theoretical method for diffraction gratings and its numerical application," J. Opt. **11**, 235–241 (1980).

134. E. F. Kuester, M. Mohamed, M. Piket-May, and C. Holloway, "Averaged transition conditions for electromagnetic fields at a metafilm," IEEE Trans. Antennas Propag. **51**, 2641–2651 (2003).

135. C. L. Holloway, A. Dienstfrey, E. F. Kuester, J. F. O'Hara, A. K. Azad, and A. J. Taylor, "A discussion on the interpretation and characterization of metafilms/metasurfaces: the two-dimensional equivalent of metamaterials," Metamaterials **3**, 100–112 (2009).

136. P. Rauter, J. Lin, P. Genevet, S. P. Khanna, M. Lachab, A. Giles Davies, E. H. Linfield, and F. Capasso, "Electrically pumped semiconductor laser with monolithic control of circular polarization," Proc. Natl. Acad. Sci. USA **111**, E5623–E5632 (2014).